PAPER

Co-assembled supramolecular hydrogels: nano-IR sheds light on tripeptide assemblies†

Paola Alletto,[a] Ana M. Garcia, [ID][b] Federica Piccirilli*[c] and Silvia Marchesan [ID] *[a]

Supramolecular hydrogels composed of self-assembling short peptides are gaining momentum for enzyme mimicry. In particular, multicomponent systems that feature similar peptides with a self-assembling motif (*e.g.*, Phe–Phe) and catalytic residues (*e.g.*, His, Asp) offer a convenient approach to organize in space, functional residues that typically occur at enzymatic active sites. However, characterisation of these systems, and especially understanding whether the different peptides co-assemble or self-sort, is not trivial. In this work, we study two-component hydrogels composed of similar tripeptides and describe how nano-IR can reveal important details of their packing, thus demonstrating it to be a useful technique to characterise multicomponent, nanostructured gels.

Introduction

Supramolecular hydrogels have attracted great interest as dynamic soft matter for a variety of potential applications, spanning from energy,[1] to medicine,[2] environmental remediation,[3] and beyond. Their matrices are composed of non-covalent interactions that provide opportunities for their modulation, formation, and dissociation on demand, using *ad hoc* stimuli.[4] In particular, the inclusion of several components is becoming popular, especially for more advanced applications, where each one can play a structural and/or functional role.[5]

However, the detailed characterisation of such systems, especially the localisation of the different components, is not always trivial. On the one hand, constituents of very different nature, such as metal nanostructures[6–8] or

[a]Department of Chemical and Pharmaceutical Sciences, University of Trieste, Via. Giorgieri 1, 34127 Trieste, Italy. E-mail: smarchesan@units.it

[b]Facultad de Ciencias y Tecnologías Químicas, Instituto Regional de Investigación Científica Aplicada (IRICA), Universidad de Castilla-La Mancha, Ciudad Real 13071, Spain

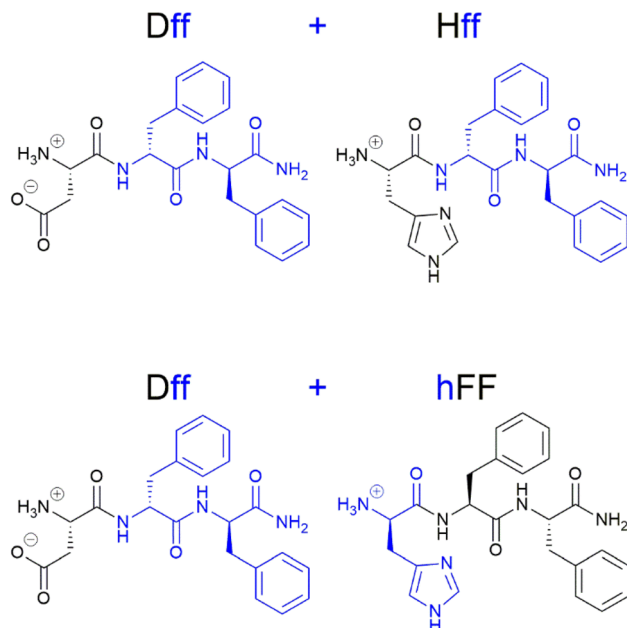*[c]Area Science Park, Padriciano 99, Trieste, Italy. E-mail: federica.piccirilli@areasciencepark.it*

nanocarbons[9–12] and organic assemblies, can be easily identified by microscopy. On the other hand, organic components are far more challenging to distinguish at the nanoscale. Furthermore, hydrogels composed of similar molecules that self-organise into nanofibrillar matrices may arise from different types of assemblies, such as those composed exclusively of either gelator through a self-sorting mechanism, or those composed of different gelators (*i.e.*, coassemblies).[13] On the one hand, self-sorting in supramolecular systems is important to enable the co-existence of distinct architectures that can function independently, and it is widely used in nature to create the required compartmentalization for complex systems; such as a living cell, to orchestrate several reactions simultaneously.[14] Self-sorted systems can display sophisticated behaviour, such as evolution in response to a trigger,[15] simultaneous targeting of multiple cell organelles,[16] and chemical signalling in protocells.[17] In the case of gels, one convenient strategy employs gelators with pH-responsive behaviour within distinct pH ranges, and/or the use of gelators that respond to different stimuli, so that specific gelation triggers can be used to exert selective control over the organization of each gelator.[18] Dynamic and evolving self-sorted gels can be obtained through accurate choice of the assembly triggers, and the mutual influence that one gelator self-organization can exert onto another.[19]

On the other hand, co-assembly can be attractive to tailor supramolecular organization towards specific properties and functions that cannot be achieved by a single component, for instance to control biomolecular conformation and stability,[20] to attain and transfer specific responses such as chiroptical switches,[21] or for synergistic behaviour, as demonstrated for example to attain broad antibacterial activity.[22] A particularly interesting approach derives from the finding that racemic mixtures of gelators can yield co-assemblies with peculiar properties, and stronger gel networks.[23] In particular, self-assembling peptides are attractive gelators, thanks to their easy modular design and synthesis, and the possibility to include diverse amino acids, thus functional groups, chirality, properties, and functions.[24] Schneider and collaborators reported in 2011 the racemic assembly of a peptide gelator with remarkably enhanced rigidity relative to gels formed by each enantiomer alone.[25] The elucidation of how the two enantiomers were interacting was very challenging, since no significant differences were found by spectroscopic or microscopic investigations. It took a few years, and an arsenal of advanced techniques, including isotope labelling and small-angle neutron scattering, to address such a formidable challenge. In 2017, Schneider and collaborators reported the finding that the two enantiomers were alternating in stacks forming a rippled-beta sheet,[26] which is a structure that had been predicted by Pauling and Corey back in 1953.[27] Interestingly, peptide stacks were held together by a network of hydrogen bonds between amide groups, whilst forming peculiar hydrophobic interactions that are nested between enantiomers in the dry interior of racemic fibrils.[26]

Inspired by these studies, we reasoned that the maximization of such hydrophobic regions could enhance hydrophobic substrate binding for catalysis and find scope in enzyme mimicry. Therefore, we took the heterochiral peptide gelator D-His-L-Phe-L-Phe-NH$_2$ (ref. 28) (hFF) and studied its co-assembly in equimolar mixtures with its enantiomer (Hff). This gelator can mimic esterases and catalyse the hydrolysis of *p*-nitrophenylacetate, a convenient chromogenic substrate,[29] only when it is present in the self-assembled state. We found that the racemic

Dff + **Hff**

Dff + **hFF**

Scheme 1 Heterochiral tripeptides studied for co-assembly in this work.

hydrogel not only displayed increased viscoelastic moduli and resistance against applied stress, as expected for a rippled-beta sheet, but also enhanced catalysis with over 50% improvement of the reaction rate under analogous conditions to the enantiopure assemblies. The presence of more hydrophobic regions in the racemic gel relative to enantiopure analogs was confirmed by ANS fluorescence.[30]

Considering that hydrolases typically feature catalytic dyads or triads, including not only His, as the above peptide sequence, but also other catalytically active residues, we thus wondered whether we could extend this approach to also include other functional residues. In particular, we focused our interest in aspartate (Asp), which is a key acidic residue in esterase catalytic sites[31] that plays key roles in proton transfer and in positioning the correct His tautomer for catalysis.[32] Furthermore, the Asp sidechain features a carboxylate group whose stretching has characteristic signals in the infrared regions corresponding to 1574–1595 (asymmetric) and 1392–1425 (symmetric).[33] While the first one falls in a crowded region where aromatic signals are also present, the latter one is in a promising range for correct identification, also in the presence of other amino acids, such as His and Phe. Combination of infrared spectroscopy with AFM analysis in a nano-IR setup could thus provide a convenient tool to investigate whether L-Asp-D-Phe-D-Phe-NH$_2$ (Dff) co-assembles with Hff or with hFF (Scheme 1).

Results and discussion

The three tripeptides Dff, Hff, and hFF were synthesised by solid-phase peptide synthesis with a standard Fmoc protection strategy, Oxyma Pure B as the coupling agent, and a Rink amide linker on 2-chlorotrityl chloride resin. They were purified

using reversed-phase HPLC, and their purity and identity were confirmed by ^{1}H- and ^{13}C-NMR and ESI-MS (see ESI†). Then, self-assembly and hydrogelation were probed with a pH trigger, which consisted of dissolving the peptides in alkaline phosphate buffer, followed by dilution with an equal volume of mildly acidic phosphate buffer to reach a neutral pH 7.0 ± 0.1. In this way, each peptide formed hydrogels at 10 mM, however, we characterised the systems at 25 mM to enable comparison with the literature.[28]

In particular, Dff gelled within a few seconds at both concentrations, while it took each enantiomer with His, ~1 h to form stable hydrogels at 10 mM, thus highlighting the favourable role of Asp for gelation. At 25 mM, Dff yielded a hydrogel with $G' = 75.1 \pm 0.02$ kPa and $G'' = 6.78 \pm 1.11$ kPa that underwent a gel-to-sol transition at ~18 Pa in stress sweeps (Fig. 1A, B and ESI†). For comparison, Hff yielded hydrogels with $G' = 34.9 \pm 3.4$ kPa and hFF with $G' = 34.3 \pm 5.0$ kPa, with both displaying moduli that dropped at ~70 Pa in stress sweeps.[30] Having established that each peptide is a gelator under analogous conditions, we analysed the rheological behaviour of their co-assemblies (Fig. 1).

Maintaining the same D–L–L stereoconfiguration in the tripeptide design resulted in hydrogels with $G' = 35.3 \pm 2.9$ kPa that withstood an applied stress of up to 70 Pa (Fig. 1D), demonstrating that addition of Dff to Hff surprisingly did
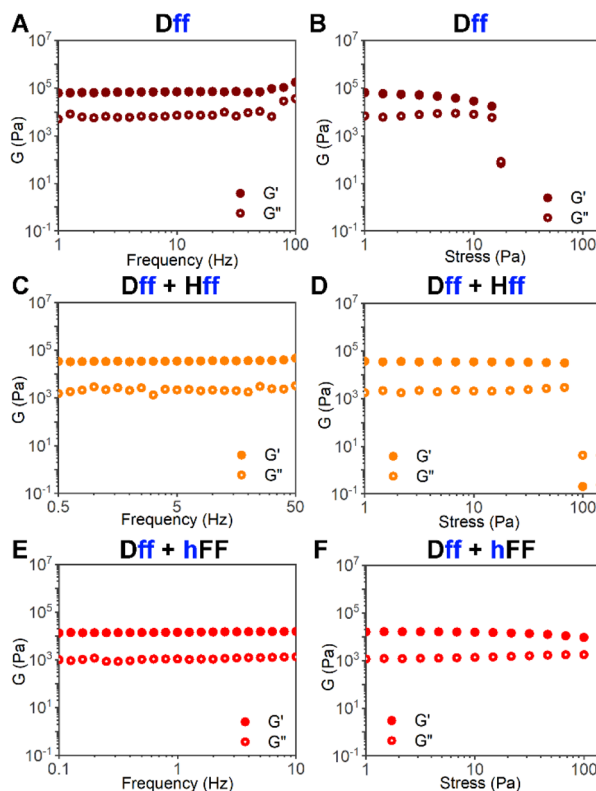

Fig. 1 Rheological analysis. Frequency sweeps (left panels) and stress sweeps (right panels) of Dff (A and B), and its co-assembled hydrogels with Hff (C and D) or hFF (E and F).

not significantly alter either its elastic modulus (Fig. 1C) or its kinetics (see ESI†). Instead, when Dff was added to the other enantiomer, hFF, the co-assembled hydrogel reached a lower elastic modulus of $G' = 15.0 \pm 0.4$ kPa, it displayed increased resistance to applied stress up to 100 Pa (Fig. 1E and F), but also significantly slower gelation kinetics (*i.e.*, ~33 min see ESI Section S4†). Thermoreversibility tests revealed a self-healing ability for all hydrogels (see ESI†). In particular, tripeptide hydrogels (25 mM) with His displayed a $T_m = 42$ °C and reformed within 20 min, while those composed of Dff had a $T_m = 55$ °C and reformed within 15 min. Dff + Hff hydrogels (25 mM each) displayed a $T_m = 58$ °C and reformed within 10 min, thus surpassing those composed of each tripeptide alone in both resistance against heating and kinetics of re-assembly. Therefore, these properties of this multicomponent hydrogel were not simply the sum of the individual components, which is in agreement with the presence of co-assembled fibrils. Analogously, when peptides with opposite stereoconfiguration were mixed (*i.e.*, Dff and hFF, 25 mM each), the T_m was similar (56 °C), while the re-assembly was slower (20 min). We inferred that the differences in the viscoelastic properties of the co-assemblies could be ascribed to more heterogeneity and defects in the supramolecular packing of Dff and hFF, which are two peptides that differ not only in the N-terminal sidechain, but also in stereoconfiguration. To verify this hypothesis, we thus undertook microscopic analysis of the co-assemblies to ascertain whether the viscoelastic differences could be correlated to nanomorphology.

Transmission electron microscopy (TEM) revealed a dense nanofibrillar network in both cases (Fig. 2A–D). However, the size distribution (Fig. 2E) was significantly wider for the gel formed by Dff and hFF, further supporting the hypothesis that changing amino acid sequence and chirality leads to higher heterogeneity within the nanofibrillar network. This finding raised the question of whether such nanomorphological diversity could be ascribed to self-sorting as opposed to co-assembly. Therefore, we sought Fourier-transformed infrared (FT-IR) spectroscopic investigations coupled to atomic force microscopy (AFM).

Firstly, we acquired attenuated total reflectance (ATR) spectra on assemblies in bulk (Fig. 3A) and compared the two-component samples to those of the individual tripeptides. Infrared spectra showed a prominent band in the 1750–1600 cm^{-1} range, mainly due to amide I modes, and a minor one peaked at 1553 cm^{-1}, ascribed to amide II modes. The comparison between the spectra revealed that the presence of Asp could be traced unambiguously by the signals in the 1400–1360 cm^{-1} range, which were ascribed to the symmetric stretching of the COO$^-$ group.[33] Conversely, the antisymmetric stretching of COO$^-$ was assigned to the shoulder at 1586 cm^{-1} that occurred in a crowded region, thus making it difficult to interpret unambiguously. The 2nd-derivative analysis (Fig. 3B) did not highlight significant differences in the amide I profiles, suggesting similarities in the overall arrangement of peptide bonds in the fibrils, as expected for β-sheets formed by this type of gelator.

To reveal finer structural details, we conducted a nanoscopic analysis by acquiring infrared spectra on single fibers imaged by AFM (see ESI†). We exploited s-SNOM spectroscopy (scattering type scanning near-field optical microscopy) that is based on the coupling of AFM to cutting-edge infrared technologies, to obtain information on nanoscale topography with chemical sensitivity. In particular, a typical s-SNOM spectrum is representative of the vibrational
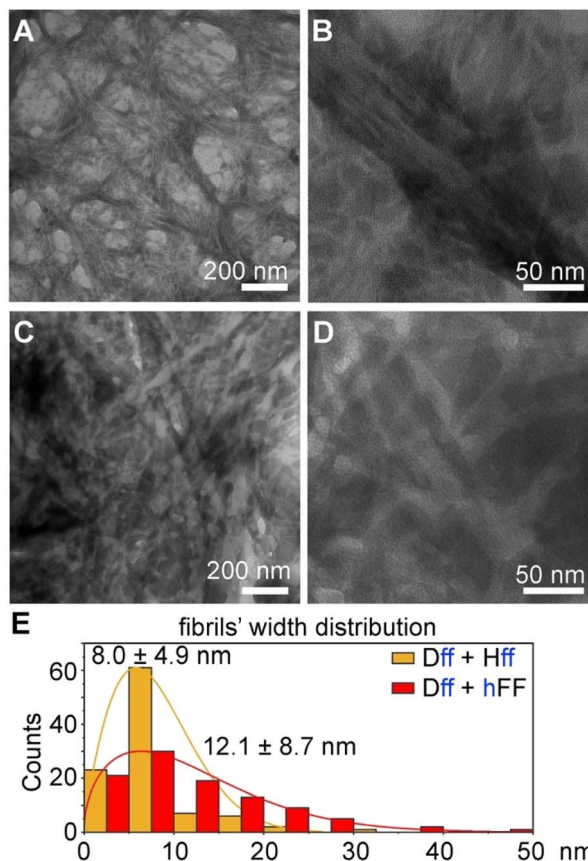
Fig. 2 TEM micrographs of Dff + Hff (A and B) and Dff + hFF (C and D) gels and their nanofibrillar width distribution (E) with mean ± standard deviation values ($n = 100$ counts).

profile of sample surfaces that are 20 nm wide, with a penetration depth of up to 100 nm.[34,35] Moreover, the interaction of the incoming radiation with the metallic tip of the AFM results in a strong polarization of the electromagnetic radiation along the direction perpendicular to the sample.[36] Thus, s-SNOM peak intensities strongly depend on the orientation of covalent bonds. Fig. 4A shows the nano-IR average absorption measured on different fibers of the two-component assemblies. Fig. 4B shows the corresponding data acquired for the racemic gel composed of Hff and hFF and devoid of the Asp signal, as a control. First of all, all spectra measured on different fibers of the two-component samples of Fig. 4A show the Asp signals, and in particular the distinctive signature below 1400 cm^{-1} that indeed is absent in the control without Asp (Fig. 4B), while it is present in the spectrum of Dff (see ESI, Section S6†). This data supports the hypothesis of co-assembled systems in both cases, as opposed to self-sorted ones, where two populations of fibers with distinctive profiles with and without Asp signals would be expected. Interestingly, despite showing similar frequency, the profile spectra showed clear differences in peak intensities. Based on ATR results, which confirmed similar absorption profiles for the different samples (Fig. 3), and given
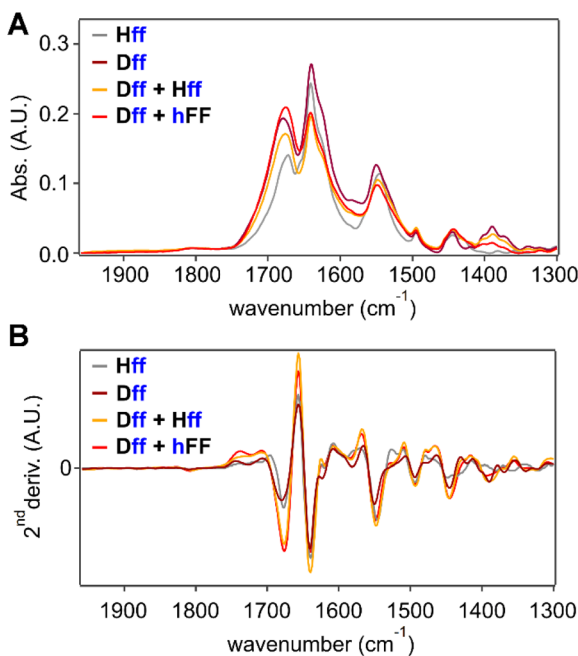
Fig. 3 ATR spectra (A) and their second derivative (B), in the amide region for the peptide gels.

the polarized nature of the s-SNOM signal, this evidence hinted at differences in the three-dimensional arrangement of the assembled tripeptides that were likely to display a strong alignment of IR-active functional groups. To deepen this aspect, we performed principal component analysis (PCA) on single nano-IR absorbance spectra, the results are shown in Fig. 4C and D. The first three components, PC1, PC2 and PC3, whose scores and loadings are shown respectively in Fig. 4C and D, were taken into account, covering respectively 38%, 16% and 14% of the total data variance. The two-component systems have been compared to the Dff assembly too (maroon markers). We first observed that Dff–Hff spectral distribution appeared to be more homogeneous compared to the other samples, as revealed by the area of the variance ellipses shown in Fig. 4C. This is likely related to a higher structural order of Dff–Hff in the assembly network compared to Dff–hFF, as expected, and surprisingly to Hff–hFF too. It is possible that the negative charge on the Asp sidechain establishes ionic interactions with the cationic N-terminal groups, thus contributing to the organisation of the assemblies. This hypothesis was further supported by ^{1}H-NMR studies, which showed significant shifts for Dff–Hff relative to spectra of the individual components (*i.e.*, Dff or Hff) at neutral pH, but not at pH 2.0, where a different ionization state is expected (see ESI, Section S7†).

Score plots revealed the clear separation of Dff-Hff from the other samples, toward positive values of PC1, of the Dff toward positive values of PC2, and of the racemic samples toward positive values of PC3. As shown in Fig. 4D, where PCA loadings are reported, PC1 shows a prominent peak around 1690–1700 cm^{-1} likely related to amide I modes[37] that have been described for primary amides (*i.e.*
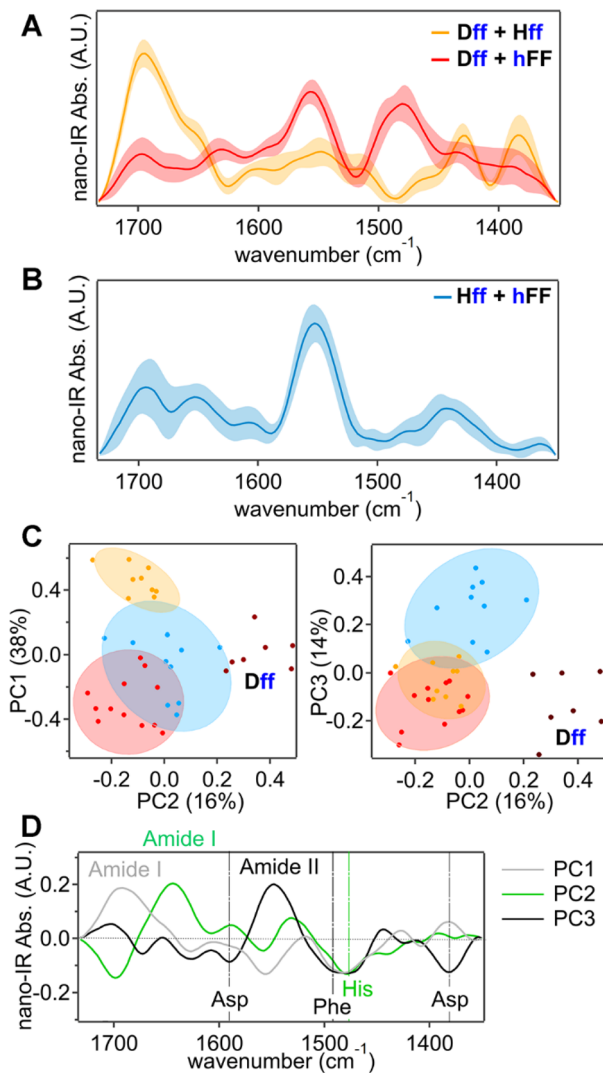
Fig. 4 Nano-IR data average profiles for the co-assembled gels (A and B) and PCA (C and D). Ellipses in C indicate 90% variance data for Dff + Hff (light orange), Dff + hFF (red), and Hff + hFF (light blue).

terminal $CONH_2$ groups),[38] or to H-bound COO^- groups.[39] PC2 scores, whose loading shows a main peak at 1645 cm^{-1}, representative of amide I modes, group together the two-component systems in a slightly negative value area, suggesting similarities in their amide 3D arrangements with damped amide I intensity compared to Dff, conversely showing positive PC2 values. Similarly to amyloid fibrils, the high alignment of amide bonds along the fiber axis indeed produced the reduction of the amide I band intensity.[40] PC3 showed a main peak at 1550 cm^{-1}, ascribed to the amide II band and minor negative contributions of Asp COO^- modes at 1586 and 1380 cm^{-1}. It can thus be considered as a fingerprint of Asp, as also suggested by the grouping together of all Asp-containing samples.

In terms of catalytic activity, the racemic co-assembled fibrils composed of Hff and hFF (each one at 12.5 mM) displayed a $k_{obs} = 7.0 \times 10^{-4}$ s^{-1} for the hydrolysis of p-nitrophenylacetate (pNPA, 1 mM) that was over 50% higher relative to that displayed by each enantiomer alone at the same overall concentration (25 mM, $k_{obs} = 5.0 \times 10^{-4}$ s^{-1}). This improvement of activity was ascribed to the increased presence of hydrophobic pockets, to accommodate the reaction substrate in the racemic rippled β-sheets, as confirmed by a fluorescence assay and molecular models.[30] In contrast, addition of an equimolar amount of Dff (25 mM) to hFF led to a $k_{obs} = 4.8 \times 10^{-4}$ s^{-1}, thus with a marginal improvement relative to the tripeptide with His alone (see ESI Section S8†). Unfortunately, the analogous mixture of Dff with Hff (same stereoconfiguration) resulted in a significantly lower $k_{obs} = 1.8 \times 10^{-4}$ s^{-1} (see ESI, Section S8†). It is plausible that the more organized packing of Dff + Hff, relative to the more disordered Dff + hFF shown by the PCA analysis on Nano-IR data and TEM data, does not accommodate the reaction substrate as well and/or that the interaction between Hff and Dff renders the catalytic sites less reactive.

Experimental

Materials and methods

All reagents and chemicals were purchased from Merck (Milan, Italy) without further purification, except for the Rink amide linker and the 2-chlorotrityl chloride resin, that were obtained from Iris Biotech GmbH (Marktredwitz, Germany). An in-line Millipore RiOs/Origin system provided MilliQ water with a resistivity higher than 18 MΩ cm. LC-MS analyses were performed on an Agilent 6120 single-quadrupole system, the ^{1}H-NMR and ^{13}C-NMR spectra were recorded at 400 MHz and 100 MHz, respectively, using a 400 MHz Varian Innova Instrument, with chemical shift reported as ppm.

Synthetic procedures

The tripeptides were prepared using solid-phase peptide synthesis using a Rink amide linker on a 2-chlorotrityl chloride resin, with standard protocols for the Fmoc-protection strategy and Oxyma Pure B as the coupling agent. The crudes of hFF and Hff were concentrated under argon flow and then dissolved in a mixture of acetonitrile (MeCN, 20%) and milliQ water (80%) with 0.05% trifluoroacetic acid (TFA), these were also the solvents used for HPLC purification. Samples were centrifuged at 15 000 rpm for 10 min, then 0.2 μm filtered prior to injection into the HPLC. Each peptide was purified on an Agilent 1260 with a C-18 column (Kinetex, 5 μm, 100 Å, 250 × 10 mm, Phenomenex), $T = 35$ °C, flow = 3 mL min^{-1} with the following method: $t = 0$–2 min, 20% MeCN (0.05% TFA); $t = 8.5$ min, 33% MeCN (0.05% TFA), $t = 11$–13 min, 95% MeCN (0.05% TFA). Rt = 6.6 min.

Dff was concentrated under argon flow and then dissolved in a mixture of acetonitrile (MeCN, 30%) and milliQ water (70%) with 0.05% trifluoroacetic acid (TFA), these were also the solvents used for HPLC purification. The sample was centrifuged at 15 000 rpm for 10 min, then 0.2 μm filtered prior to injection into the HPLC. The peptide was purified on an Agilent 1260 with a C-18 column (Kinetex, 5 μm, 100 Å, 250 × 10 mm, Phenomenex), $T = 35$ °C, flow = 3 mL min^{-1} with the following method: $t = 0$–2 min, 30% MeCN (0.05% TFA); $t = 15$ min, 56%

Faraday Discussions

MeCN (0.05% TFA), $t = 15$–18 min, 95% MeCN (0.05% TFA), $t = 18$–20 min, 95% MeCN (0.05% TFA). Rt = 4.7 min.

Self-assembly protocol

Tripeptides were dissolved in sodium phosphate (0.1 M, pH 11.8) at double the desired concentration, and then the resulting solutions were diluted with an equal volume of mildly acidic sodium phosphate (0.1 M, pH 5.6) to reach a final pH 7.0 ± 0.1 and a final concentration of 25 mM for each tripeptide, unless otherwise stated in the text.

Oscillatory rheology

Hydrogels were freshly prepared *in situ* on a 20 mm wide steel plate with parallel geometry of a Malvern Kinexus Ultra Plus Rheometer (Alfatest, Milan, Italy) equipped with a Peltier temperature controller. Time sweeps were performed at 1 Hz and 1 Pa at 25 °C. Frequency sweeps were performed at 1 Pa and 25 °C. Stress sweeps were registered at 1 Hz and 25 °C.

TEM analysis

Samples were freshly prepared and after one hour they were deposited on carbon grids (200 mesh, copper) and dried *in vacuo*. TEM analyses were performed on a TEM Philips EM208, using an acceleration voltage of 100 kV, equipped with a Quemesa camera (Olympus). Image analysis was performed with FIJI software.

ATR measurements

Infrared analysis was performed at the offline experimental station of SISSI-Bio beamline of Elettra Sincrotrone Trieste.[41] Samples were measured in powder form. Measurements were carried out using a Vertex70v interferometer equipped with a single reflection monolithic Diamond ATR crystal (platinum, Bruker Optics) and a DTGS (deuterated triglycine sulphate) detector, working at a speed of 7.5 kHz and a KBr beamsplitter. The interferometric setup was used in combination with a glow-bar source allowing access to the spectral region between 1000 and 4000 cm^{-1}. For each spectrum, 256 scans were accumulated and averaged for each sample, Fourier transformed, then referenced with the spectrum of the clean ATR crystal. The Fourier Transform was performed by applying a 3-terms Blackman Harris apodization filter.

Nano-IR spectroscopy

The nanoscale analysis was done taking advantage of infrared nanoscopy. To this aim, 5 μL of sample was dropped onto gold-coated silicon wafers then dried in a vacuum. The measurements were performed at the SISSI-Bio infrared beamline of Elettra Sincrotrone Trieste taking advantage of a Neascope microscope (Atto-cube System AG), equipped with a scattering-type scanning near field optical microscopy (SNOM) module. Arrow type, AFM tips high sensitivity, 20 nm wide and coated with PtIr (Neaspec GmbH, Munich) were exploited to collect the scattered IR signal. The microscope was operated in tapping mode with a canti-lever frequency of 232 kHz and a free amplitude of oscillation around 100 nm. The DFG (difference frequency generation) laser was set to emit in the spectral region

$1000–2000$ cm^{-1}, with maximum emission at 1666 cm^{-1}. The usable spectral window allowed to access both amide and lateral chain modes.[33,42] Spectra were acquired at a resolution of 8 cm^{-1} with each measurement taking ∼3 min. A clean gold surface was used as a reference to calculate the nano-IR absorbance. Neaplot (Attocube System AG, Munich) software was used for spectroscopic data analyses and topographic imaging maps were analyzed with Gwyddion 2.59. The 2nd-harmonic of optical phase signal was considered for nano-IR absorbance curves. Principal component analysis was performed on nano-IR absorption spectra thanks to the use of Quasar 1.7.0.[43] A preprocessing procedure was applied to all spectra comprising a cut of spectra between $1720–1350$ cm^{-1}, rubber-band baseline correction, vector normalization and 15-points smoothing. Variance ellipses were built by considering 90% of the total variance for each sample.

Thermoreversibility tests

Thermoreversibility tests were performed using a water-bath on a hot-plate stirrer with a temperature controller, by heating the vials with hydrogels up to the melting temperature, and then by letting them cool down to room temperature on the lab bench.

NMR spectra

^{1}H- and ^{13}C-NMR spectra were acquired at 400 MHz and 100 MHz, respectively, using a 400 MHz Varian Innova Instrument, with chemical shift reported in ppm, in deuterated solvents as indicated in the ESI.† pH was adjusted with NaOH 1 M to 7, or with HCl 1 M to 2, for spectra shown in the ESI, Section S7.†

Catalytic activity

Catalytic activity was assessed as previously described.[30]

Conclusions

This work demonstrates that it is possible to expand the design of multicomponent supramolecular hydrogels in minimalistic tripeptides, by including sequences with the Phe–Phe motif to promote self-organisation, that differ not only in the third amino acidic residue, but also in overall stereoconfiguration. In particular, binary systems featuring His–Phe–Phe and Asp–Phe–Phe, either with the same or with the opposite stereoconfiguration, were successfully co-assembled into nanofibrillar hydrogels. The viscoelastic behaviour of these systems showed that adding Dff to Hff resulted in dramatically faster gelation kinetics, albeit the elastic modulus and the hydrogel resistance against the applied stress were similar. We inferred that the negative charge of the Asp sidechain played a favourable role in the self-organisation, likely establishing electrostatic interactions with the cationic N-terminal ammonium groups, as supported by NMR data suggestive of interactions between the two shifting His signals. Conversely, also changing the stereoconfiguration of the components in the hydrogels obtained from Dff and hFF, significantly slowed down gelation, suggesting that self-organisation was more difficult in this case. The hydrogels displayed lower elastic modulus that suggested more defects in the

supramolecular packing. The high heterogeneity of Dff–hFF samples was found also in terms of the nanofibril widths' wider distribution relative to Dff–Hff, that appeared more homogeneous. Nano-IR data confirmed lower variance in the latter sample, and it provided useful insights into the packing modes, suggesting co-assembly into amyloid-like fibers in all the two-component systems. Overall, we find this technique very useful to characterise multicomponent and supra-molecular hydrogels and to reveal fine structural details that can discriminate between self-sorting and co-assembling gelators.

Data availability

The data supporting this article have been included as part of the ESI.†

Author contributions

P. A. – investigation. A. M. G., F. P., S. M. – resources and supervision. All authors contributed to data analysis and writing of the MS.

Conflicts of interest

There are no conflicts to declare.

Acknowledgements

Notes and references

1 O. Dumele, J. Chen, J. V. Passarelli and S. I. Stupp, *Adv. Mater.*, 2020, **32**, 1907247.
2 L. Rijns, M. B. Baker and P. Y. W. Dankers, *J. Am. Chem. Soc.*, 2024, **146**, 17539–17558.
3 A. M. Gutierrez, E. M. Frazar, M. V. X. Klaus, P. Paul and J. Z. Hilt, *Adv. Healthcare Mater.*, 2022, **11**, 2101820.
4 M. Neumann, G. di Marco, D. Iudin, M. Viola, C. F. van Nostrum, B. G. P. van Ravensteijn and T. Vermonden, *Macromolecules*, 2023, **56**, 8377–8392.

5 B. O. Okesola, Y. Wu, B. Derkus, S. Gani, D. Wu, D. Knani, D. K. Smith, D. J. Adams and A. Mata, *Chem. Mater.*, 2019, **31**, 7883–7897.

6 S. Adorinni, S. Gentile, O. Bellotto, S. Kralj, E. Parisi, M. C. Cringoli, C. Deganutti, G. Malloci, F. Piccirilli, P. Pengo, L. Vaccari, S. Geremia, A. V. Vargiu, R. De Zorzi and S. Marchesan, *ACS Nano*, 2024, **18**, 3011–3022.

7 J. K. Wychowaniec, H. Saini, B. Scheibe, D. P. Dubal, A. Schneemann and K. Jayaramulu, *Chem. Soc. Rev.*, 2022, **51**, 9068–9126.

8 D. Cohen-Gerassi, O. Messer, G. Finkelstein-Zuta, M. Aviv, B. Favelukis, Y. Shacham-Diamand, M. Sokol and L. Adler-Abramovich, *Adv. Healthcare Mater.*, 2024, **13**, 2303632.

9 V. Wulf and G. Bisker, *ACS Nano*, 2024, **18**, 29380–29393.

10 D. Marin, M. Bartkowski, S. Kralj, B. Rosetti, P. D'Andrea, S. Adorinni, S. Marchesan and S. Giordani, *Nanomaterials*, 2022, **13**, 172.

11 C. Ligorio, M. Zhou, J. K. Wychowaniec, X. Zhu, C. Bartlam, A. F. Miller, A. Vijayaraghavan, J. A. Hoyland and A. Saiani, *Acta Biomater.*, 2019, **92**, 92–103.

12 C. Guilbaud-Chéreau, B. Dinesh, L. Wagner, O. Chaloin, C. Ménard-Moyon and A. Bianco, *Nanomaterials*, 2022, **12**, 1643.

13 C. Colquhoun, E. R. Draper, E. G. B. Eden, B. N. Cattoz, K. L. Morris, L. Chen, T. O. McDonald, A. E. Terry, P. C. Griffiths, L. C. Serpell and D. J. Adams, *Nanoscale*, 2014, **6**, 13719–13725.

14 M. M. Safont-Sempere, G. Fernández and F. Würthner, *Chem. Rev.*, 2011, **111**, 5784–5814.

15 X. Liu, F. Tian, Z. Zhang, J. Liu, S. Wang, R.-C. Guo, B. Hu, H. Wang, H. Zhu, A.-A. Liu, L. Shi and Z. Yu, *J. Am. Chem. Soc.*, 2024, **146**, 24177–24187.

16 X. Liu, M. Li, J. Liu, Y. Song, B. Hu, C. Wu, A.-A. Liu, H. Zhou, J. Long, L. Shi and Z. Yu, *J. Am. Chem. Soc.*, 2022, **144**, 9312–9323.

17 W. Mu, L. Jia, M. Zhou, J. Wu, Y. Lin, S. Mann and Y. Qiao, *Nat. Chem.*, 2024, **16**, 158–167.

18 E. R. Draper, E. G. B. Eden, T. O. McDonald and D. J. Adams, *Nat. Chem.*, 2015, **7**, 848–852.

19 C. Tangsombun and D. K. Smith, *Chem. Mater.*, 2024, **36**, 5050–5062.

20 C. Zhao, X. Li, X. Han, Z. Li, S. Bian, W. Zeng, M. Ding, J. Liang, Q. Jiang, Z. Zhou, Y. Fan, X. Zhang and Y. Sun, *Nat. Commun.*, 2024, **15**, 1488.

21 D. Han and T. Jiao, *Langmuir*, 2022, **38**, 13668–13673.

22 B. Das Gupta, A. Halder, T. Vijayakanth, N. Ghosh, R. Konar, O. Mukherjee, E. Gazit and S. Mondal, *J. Mater. Chem. B*, 2024, **12**, 8444–8453.

23 K. Liu, H. Cao, W. Yuan, Y. Bao, G. Shan, Z. L. Wu and P. Pan, *J. Mater. Chem. B*, 2020, **8**, 7947–7955.

24 D. A. Scott, A. Wasmuth, E. Abelardo, K. L. Hudson, A. R. Thomson, M. A. Birchall, N. Mehrban, J. M. Henley and D. N. Woolfson, *Adv. Funct. Mater.*, 2024, **34**, 2410333.

25 K. J. Nagy, M. C. Giano, A. Jin, D. J. Pochan and J. P. Schneider, *J. Am. Chem. Soc.*, 2011, **133**, 14975–14977.

26 K. Nagy-Smith, P. J. Beltramo, E. Moore, R. Tycko, E. M. Furst and J. P. Schneider, *ACS Cent. Sci.*, 2017, **3**, 586–597.

27 L. Pauling and R. B. Corey, *Proc. Natl. Acad. Sci. U. S. A.*, 1953, **39**, 253–256.

28 M. Kurbasic, A. M. Garcia, S. Viada and S. Marchesan, *Molecules*, 2020, **26**, 173.

29 P. Janković and D. Kalafatovic, in *Methods in Enzymology*, ed. I. V. Korendovych, Academic Press, 2024, vol. 697, pp. 423–433.

30 M. C. Mañas-Torres, P. Alletto, S. Adorinni, A. V. Vargiu, L. Alvarez De Cienfuegos and S. Marchesan, *Org. Biomol. Chem.*, 2025, **23**, 2797–2801.

31 C. S. Craik, S. Roczniak, C. Largman and W. J. Rutter, *Science*, 1987, **237**, 909–913.

32 K. D. Cramer and S. C. Zimmerman, *J. Am. Chem. Soc.*, 1990, **112**, 3680–3682.

33 A. Barth, *Prog. Biophys. Mol. Biol.*, 2000, **74**, 141–173.

34 F. Huth, A. Govyadinov, S. Amarie, W. Nuansing, F. Keilmann and R. Hillenbrand, *Nano Lett.*, 2012, **12**, 3973–3978.

35 A. Caldiroli, S. Cappelletti, G. Birarda, A. Redaelli, S. Adele Riboldi, C. Stani, L. Vaccari and F. Piccirilli, *Analyst*, 2023, **148**, 3584–3593.

36 A. Cvitkovic, N. Ocelic and R. Hillenbrand, *Opt. Express*, 2007, **15**, 8550–8565.

37 A. Mauerer and G. Lee, *Eur. J. Pharm. Biopharm.*, 2006, **62**, 131–142.

38 V. A. Lorenz-Fonfria, *Chem. Rev.*, 2020, **120**, 3466–3576.

39 R. Dunmur and M. Murray, IR Absorptions of Double Bonds, in *Spectroscopic Methods in Organic Chemistry*, ed. M. Hesse, H. Meier and B. Zeeh, Thieme, Stuttgart (Germany), 2nd edn, 2008, ch. 9.

40 I. Amenabar, S. Poly, W. Nuansing, E. H. Hubrich, A. A. Govyadinov, F. Huth, R. Krutokhvostov, L. Zhang, M. Knez, J. Heberle, A. M. Bittner and R. Hillenbrand, *Nat. Commun.*, 2013, **4**, 2890.

41 G. Birarda, D. Bedolla, F. Piccirilli, C. Stani, H. Vondracek and L. Vaccari, *SPIE Annual meeting*, 2022, vol. 11957, pp. 1195707.

42 A. Barth and C. Zscherp, *Q. Rev. Biophys.*, 2002, **35**, 369–430.

43 https://quasar.codes, accessed on 14th Feb 2025.